

# Black Hole - Neutron Star Binary Mergers: The Impact of Stellar Compactness

Bing-Jyun Tsao, Bhavesh Khamesra, Miguel Gracia-Linares,  
Pablo Laguna

Center for Gravitational Physics, Department of Physics, The University of Texas at Austin, Austin, TX 78712, U.S.A.

**Abstract.** Recent gravitational wave observations include possible detections of black hole - neutron star binary mergers. As with binary black hole mergers, numerical simulations help characterize the sources. For binary systems with neutron star components, the simulations help to predict the imprint of tidal deformations and disruptions on the gravitational wave signals. In a previous study, we investigated how the mass of the black hole has an impact on the disruption of the neutron star and, as a consequence, on the shape of the gravitational waves emitted. We extend these results to study the effects of varying the compactness of the neutron star. We consider neutron star compactness in the 0.123 to 0.2 range for binaries with mass ratios of 3 and 5. As the compactness and the mass ratio increase, the binary system behaves during the late inspiral and merger more like a black hole binary. For the case with the highest mass ratio and most compact neutron star, the gravitational waves emitted, in terms of mismatches, are almost indistinguishable from those by a binary black hole. The disruption of the star significantly suppresses the kicks on the final black hole. The disruption also affects, although not dramatically, the spin of the final black hole. Lastly, for neutron stars with low compactness, the quasi-normal ringing of the black hole after the merger does not show a clean quasi-normal ringing because of the late accretion of debris from the neutron star.

## 1. Introduction

The most recent catalogue of gravitational wave (GW) observations (GWTC-3) from the LIGO-VIRGO-KAGRA (LVK) collaboration contain three possible neutron star - black hole (NSBH) binary mergers (GW191219\_163120, GW200115\_042309, and GW200210\_092254) [1]. As the detectors increase their sensitivity, the number of NSBH, and also binary neutron star (BNS) merger detections will increase. As with mergers of binary black holes (BBHs), waveform from numerical simulations are important in characterizing the sources (masses, spins, eccentricity, etc.), and for the case of binaries with neutron star (NS) components, simulations provide extremely valuable information about the internal structure of the NS and the effects from tidal deformations and disruptions.

Several numerical studies of NSBH mergers that include the effects of tidal deformations and disruption effects have been done in the past decade. To study the effect of mass ratio  $q = M_h/M_*$  and compactness  $C = M_*/R_*$  where  $M_*$  and  $R_*$  are respectively the mass and radius of the NS and  $M_h$  the mass of the black hole (BH), Shibata *et al* [2] probed mass ratios  $1.5 \leq q \leq 5$  and compactnesses  $0.145 \leq C \leq 0.178$  and found that low compactness and mass ratio result in larger NS disruption. Duez *et al* [3] investigated a polytropic equation of state (EOS)  $P = K\rho_0^\Gamma$  with adiabatic index  $\Gamma = 2, 2.75$  and two cases of nuclear-theory based Shen EOS. With fixed compactness of  $C = 0.15$ , the cases varying EOS stiffness showed a limited effect on the total mass remnant, approximately 7% of tidal debris outside BH at the end of the simulation. However, the effect of stiffer EOS manifests in a more massive, larger, and longer-lived tidal tail. Kyutoku *et al* [4] studied mixed binaries with non-spinning BHs and piecewise-polytropic EOSs, with one piece for the core and another for the crust as given in [5]. Spinning BHs were considered in [6]. The studies found the effects of the EOSs on tidal disruption in two aspects: First, NSs with stiffer EOS have a larger radius and thus less compactness, yielding stronger disruption. Second, with fixed compactness, the comparison of different adiabatic index of the core showed that more centrally condensed density profile (higher adiabatic index) would result in a smaller mass remnant. Etienne *et al* [7] studied cases with aligned, anti-aligned, and zero BH spins. The study found that massive disk ( $\sim 0.2M_\odot$ ) can be formed for the aligned and highly-spinning (dimensionless BH spin  $a = 0.75$ ) case, whereas only small disks are formed for the anti-aligned cases. The effect of spin was investigated also by Kyutoku *et al* [6]. The study found that for aligned cases, higher spin magnitudes enhances the NS disruption and leads to more remnant mass. An enormous disk up to  $0.5M_\odot$  is obtained by Foucart *et al* [8] as they pushed the BH spin up to  $a = 0.9$ . In the same study they also found that the misalignment angle has a strong affect on the remnant mass only for large angles  $> 40^\circ$  relative to the orbital angular momentum. The magnetic field is also a factor affecting the remnant mass. Etienne *et al* [9] performed full GRMHD simulations with a poloidal magnetic field. The study showed that the only cases where the magnetic field has significant impact on the remnant mass are when the maximum initial seeded field reaches  $\sim 10^{17}G$ . In a follow up study [10], a tilted poloidal magnetic field in the NS was shown to lead to magnetic rotation instability, producing an outflow powerful enough to generate sGRBs. Using 26 numerical simulations, Foucart [11] constructed a model to predict the mass remnant by comparing the tidal radius to the ISCO radius of the system given its parameters.

In our previous study [12], we investigated the impact that the mass ratio has on the merger dynamics and the GWs emitted for polytropic EOS. Specifically, we studied how as the mass ratio increases, the less mass ejecta is released, and the system behaves more like a BBH system. As observed in Ref. [13], the final fate of NSBH binaries is determined by not only the mass ratio but also the compactness of the NS. The main objective of the present work is to explore the effects of the compactness of the NS from situations in which the NS is deformed as it merges with the BH to cases when the

NS is completely disrupted by the BH before the merger. One motivation for carrying out this study is to test the ability of our initial data framework, an extension of the Bowen-York methods for BBH merger, to model NSBH systems.

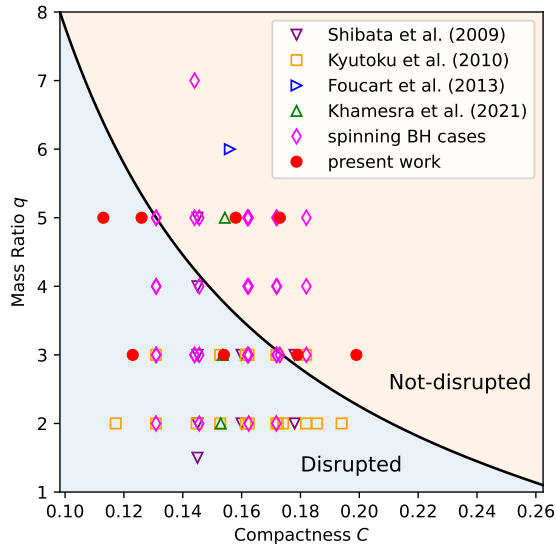


Figure 1: The solid line denotes the boundary between NSBH mergers in which the star is swallowed by the BH almost undisturbed (orange region) and those binaries in which the star is disrupted before the merger (blue region).

The parameter space under consideration is two-dimensional and consists of the mass ratio  $q$  and compactness  $C$ . As depicted in Figure 1, there are two regions: values of  $q$  and  $C$  for which the star disrupts before the merger (blue region) and values for which the NS remains basically intact before it is swallowed by the BH (orange region). To get a rough estimate of the boundary separating these regions, we recall that the tidal radius  $r_t$  is the separation at which the tidal force  $M_h M_* R_* / r_t^3$  by the BH equals the star's self-gravity  $M_* / R_*^2$ . This yields  $C^3 = q^{-2} (M_h / r_t)^3$ . A good approximation to the minimum tidal radius for which the NS disrupts is the radius of the inner-most stable circular orbit (ISCO), which for a point particle orbiting a non-rotating BH is  $6 M_h$ . Thus, the boundary between disruption and non-disruptions is given by  $(6C)^{3/2} q = 1$ . A more accurate expression, which is depicted in Fig. 1 with a black line, was obtained by Taniguchi *et al* [14] using results from numerical simulations. The expression reads

$$(6C)^{3/2} q = 3.7 (1 + 1/q)^{-3/2} [1 - 0.444 q^{-1/4} (1 - 3.54 C^{1/3})] . \quad (1)$$

In Fig. 1, with green triangles we denote the simulations in our previous work [12], and with red dots the simulations for the present study. The figure also includes the simulations by Kyutoku *et al* [4], Shibata *et al* [2], Foucart *et al* [15], and cases with spinning black holes [7, 6, 8, 16]. That is, our present study considers the regime of 0.11 to 0.20 compactness for mass ratio  $q = 3$  and  $q = 5$  to find distinguishing properties separating disrupted and non-disrupted mixed binaries.

The paper is organized as follows: A summary of the method to construct initial data for binary systems with NSs is presented in Section 2. Numerical setup, simulation parameters, and convergence tests are given in Section 3. Results are presented and discussed in Section 4, with conclusions in Section 5. Quantities are reported in units of  $M = M_h + M_*$ , with  $G = c = 1$ . Space-time signature is  $(-+++)$ , and tensor indices are denoted with Latin letters from the beginning of the alphabet. Spatial tensor indices are denoted with Latin letters from the middle of the alphabet.

## 2. Initial Data for Binary Systems with Neutron Stars

In Ref. [17], we introduced a method to construct initial data for NSBH binaries following parallel steps to the Bowen-York approach for BBH initial data with BHs modeled as punctures. The initial data is comprised of the spatial metric  $\gamma_{ij}$  and the extrinsic curvature  $K_{ij}$  of the initial space-like hypersurface. For the matter sources, the data involves

$$\rho_H \equiv n^a n^b T_{ab} \quad (2)$$

$$S^i \equiv -\gamma^{ij} n^b T_{jb}, \quad (3)$$

where  $T_{ab}$  is the stress-energy tensor and  $n^a$  is the unit time-like normal to the hypersurface.  $\rho_H$  and  $S^i$  are respectively the energy and momentum density measured by normal  $n^a$  observers. We consider a perfect fluid for which

$$T_{ab} = (\rho + p)u_a u_b + p g_{ab}, \quad (4)$$

with  $\rho$  the total energy density,  $p$  the pressure,  $u^a$  the four velocity of the fluid, and  $g_{ab} = \gamma_{ab} - n_a n_b$  the space-time metric. With this,

$$\rho_H = (\rho + p)W^2 - p \quad (5)$$

$$S^i = (\rho + p)W u^i, \quad (6)$$

where  $W = -n_a u^a$  is the Lorentz factor, also given by

$$W^2 = \frac{1}{2} \left( 1 + \sqrt{1 + \frac{4S_i S^i}{(\rho + p)^2}} \right). \quad (7)$$

The initial data  $\{\gamma_{ij}, K_{ij}, \rho_H, S^i\}$  is not freely specifiable. The data must satisfy

$$R + K^2 - K_{ij} K^{ij} = 16\pi\rho_H \quad (8)$$

$$\nabla_j (K^{ij} - \gamma^{ij} K) = 8\pi S^i, \quad (9)$$

which are respectively the Hamiltonian and Momentum constraints. In these equations,  $R$  is the Ricci scalar and  $\nabla_j$  is the covariant derivative associated with  $\gamma_{ij}$ .

Eqs.(8) and (9) are solved using the conformal-transverse-traceless (CTT) approach pioneered by Lichnerowicz [18], York, and collaborators [19] in which

$$\gamma_{ij} = \psi^4 \tilde{\gamma}_{ij} \quad (10)$$

$$K_{ij} = A_{ij} + \frac{1}{3}\gamma_{ij} K \quad (11)$$

$$A^{ij} = \psi^{-10} \tilde{A}^{ij} \quad (12)$$

$$\tilde{\rho}_H = \rho_H \psi^8 \quad (13)$$

$$\tilde{S}^i = S^i \psi^{10}. \quad (14)$$

From the last two transformations, we get that  $\tilde{\rho} = \rho \psi^8$ ,  $\tilde{p} = p \psi^8$ ,  $\tilde{u}^i = u^i \psi^2$  and  $\tilde{W} = W$ .

As commonly done, we impose conformal flatness ( $\tilde{\gamma}_{ij} = \eta_{ij}$ ), maximal slicing ( $K = 0$ ), and  $\tilde{A}_{ij}^{\text{TF}} = 0$ . Thus, the Hamiltonian and momentum constraints become:

$$\tilde{\Delta} \psi + \frac{1}{8} \psi^{-7} \tilde{A}_{ij} \tilde{A}^{ij} = -2\pi \psi^{-3} \tilde{\rho}_H \quad (15)$$

$$\tilde{\nabla}_j \tilde{A}^{ij} = 8\pi \tilde{S}^i. \quad (16)$$

Bowen and York [20] found that a point-source (puncture) solution to  $\tilde{\nabla}_j \tilde{A}^{ij} = 0$  representing BHs with linear momentum  $P^i$  is given by:

$$\tilde{A}^{ij} = \frac{3}{2r^2} [2P^{(i}l^{j)} - (\eta^{ij} - l^i l^j) P_k l^k] \quad (17)$$

where  $l^i = x^i/r$  is a unit radial vector. Bowen [21] also found the following solution to Eq. (16) for a spherically symmetric source  $S^i$  representing an extended object with linear momentum  $P^i$ :

$$\begin{aligned} \tilde{A}^{ij} &= \frac{3Q}{2r^2} [2P^{(i}l^{j)} - (\eta^{ij} - l^i l^j) P_k l^k] \\ &+ \frac{3C}{r^4} [2P^{(i}l^{j)} + (\eta^{ij} - 5l^i l^j) P_k l^k] \end{aligned} \quad (18)$$

where

$$Q = 4\pi \int_0^r \sigma \bar{r}^2 d\bar{r} \quad (19)$$

$$C = \frac{2\pi}{3} \int_0^r \sigma \bar{r}^4 d\bar{r}. \quad (20)$$

The source function  $\sigma$  is a radial functions with compact support  $r \leq R$  such that  $\tilde{S}^i = P^i \sigma$ . Outside the source,  $Q = 1$  and  $C = 0$ , and the extrinsic curvature (18) reduces to (17). Since  $\tilde{S}^i = (\tilde{\rho} + \tilde{p})W \tilde{u}^i$ , we set  $\sigma = (\tilde{\rho} + \tilde{p})/\mathcal{K}$  with

$$\mathcal{K} = 4\pi \int_0^R (\tilde{\rho} + \tilde{p}) r^2 dr. \quad (21)$$

Thus,  $P^i = W \mathcal{K} \tilde{u}^i$ .

Given (18) for a NS and (17) for a BH, we solve the Hamiltonian constraint (15), assuming that the conformal factor has the form  $\psi = 1 + m_p/(2r) + u$  where  $m_p$  is the bare or puncture mass of the BH. To solve (15), we use the `TwoPunctures` code [22], that has been modified to handle the source  $\tilde{\rho}_H$ . To obtain initial data representing a NSBH binary system with a BH with irreducible mass  $M_h$  and a NS with mass  $M_*$ , one follows similar steps to that for BBHs. That is, one selects the target values for  $M_*$  and  $M_h$ . Next, one carries out iterations solving the Hamiltonian constraint until the target values for  $M_h$  and  $M_*$  are obtained. After each Hamiltonian constraint solve iteration, one computes  $M_h$  from the irreducible mass of the BH from its horizon. The challenge

is in finding an appropriate definition for  $M_*$ . Options are the ADM mass  $\mathcal{M}_A$  or the rest mass  $\mathcal{M}_0$  of the NS at rest in isolation, which in isotropic coordinates read

$$\mathcal{M}_A = 4\pi \int_0^R \rho \psi^5 r^2 dr \quad (22)$$

$$\mathcal{M}_0 = 4\pi \int_0^R \rho_0 \psi^6 r^2 dr \quad (23)$$

respectively, with  $\rho_0$  the rest-mass density. The approach followed in Ref. [17] was to compute  $M_*$  at iteration  $n$  from  $M_*^{(n)} = \xi^{(n-1)} M_0^{(n)}$  where  $\xi^{(n-1)} = \mathcal{M}_A^{(n-1)} / \mathcal{M}_0^{(n-1)}$  and

$$M_0 = \int \rho_0 W \sqrt{\gamma} d^3x = \int \tilde{\rho}_0 W \psi^{-2} d^3x. \quad (24)$$

At  $n = 1$ , we set  $M_*^{(1)} = \mathcal{M}_A^{(1)}$ . At the end of the iterations, we obtain the rest mass density and puncture mass that generates desired  $M_h$  and  $M_*$ .

### 3. Simulations parameters, numerical setup, and convergence tests

We set the target mass of the NS in the binary to  $M_* = 1.35 M_\odot$ . With this mass and the range of compactness  $0.113 \leq C \leq 0.199$ , the NSs have radius  $10.2 \text{ km} \leq R_* \leq 17.8 \text{ km}$ . Also, with this NS mass, the BH has a mass  $M_h = 4.05 M_\odot$  for  $q = 3$  and  $M_h = 6.75 M_\odot$  for  $q = 5$ . We model the NS as a polytrope with an equation of state  $P = K \rho_0^\Gamma$  with  $\Gamma = 2$ . Table 1 provides the NS radius  $R_*$ , central density  $\rho_c$ , ADM mass  $\mathcal{M}_A$  and rest mass  $\mathcal{M}_0$  of the NS in isolation, as well as the polytropic constant  $K$  and the grid resolution  $\Delta$  inside the NS for each compactness case. At the beginning of the simulation, all the binary systems we consider have a coordinate separation of  $9M$ . As with BBH initial data, the initial momentum of the BH and NS are obtained by integrating the post-Newtonian equations of motion from a large separation and stopping the integration when the binary separation is  $9M$ .

The system of spacetime and hydrodynamics equations are solved with `MAYA` code [23, 24, 25], our local version of the `Einstein Toolkit` code [26]. The Einstein equations are solved with the BSSN-Chi formulation [27, 28, 29]. The general relativistic hydrodynamics equations are solved following the formulation in the `Whisky` public code [30, 31, 32]. To evolve the spacetime, we use the moving puncture gauge [33, 34]. The BH is tracked with the `AHFinderDirect` code [35]. The NS is tracked via the `VolumeIntegrals` thorn [26], which locates the NS from the center of mass within a box encasing the star. The mass, spins, and multipole moments of the BH are computed using the `QuasiLocalMeasures` thorn [36] based on the dynamical horizons framework [37]. The GW strain is obtained from the Weyl scalar  $\Psi_4$  [36, 38, 39]. To compute the radiated quantities, we follow the method developed in [40]. The calculations of  $\Psi_4$ , the strain, and the radiated quantities are computed using the Python library `mayawaves` [41].

We use the moving box mesh refinement approach as implemented by `Carpet` [42]. To ensure uniformity of the resolution across the runs, we follow conditions based on

$C$	$R_*(km)$	$\rho_c(gr/cm^3)$	$\mathcal{M}_A(M_\odot)$	$\mathcal{M}_0(M_\odot)$	$K(km^2)$	$\Delta(m)$
$q = 3$						
0.123	16.834	4.65e+14	1.398	1.487	276.101	302.53
0.152	13.492	9.11e+14	1.393	1.503	204.796	236.52
0.179	11.459	1.51e+15	1.389	1.514	172.085	192.52
0.199	10.285	2.13e+15	1.385	1.519	159.252	167.77
$q = 5$						
0.113	18.728	3.44e+14	1.428	1.512	327.231	346.54
0.126	16.699	4.87e+14	1.427	1.521	276.101	305.28
0.158	13.263	9.83e+14	1.423	1.539	204.306	235.15
0.173	12.114	1.30e+15	1.420	1.545	185.431	210.40

Table 1: Compactness  $C$ , NS radius  $R_*$ , central density  $\rho_c$ , ADM mass  $\mathcal{M}_A$  and rest mass  $\mathcal{M}_0$  of the NS in isolation, as well as the polytropic constant  $K$  and the grid resolution  $\Delta$  inside the NS.

the analysis in Ref. [13], which suggested that the grid spacing inside the BH should be smaller than  $\Delta \sim M_h/20$  and inside the NS smaller than  $\Delta \sim R_*/40$ . To meet this requirement, we use 8 levels of refinement on the star. The star is covered by  $96^3$  points, with  $116^3$  points in the coarsest level. The finest refinement has an extent of  $2.4 R_*$ . At the BH we add another level of refinement. For wave extraction, we set up a sphere at radius  $130 M$  from the center of mass of the binary to capture  $\Psi_4$  and the radiated quantities.

For convergence tests, we focus on the most compact case  $C = 0.173$  for mass ratio  $q = 5$ . Our previous work [12] showed convergence tests for  $q = 2$  and 3. In this work, we carried out three simulations with resolutions in the finest mesh at the NS of  $\Delta_h = 188$  meters (high),  $\Delta_m = 210$  meters (medium), and  $\Delta_l = 339$  meters (low). Top panels in Figure 2 show the amplitude (left) and phase (right) for the three simulations. Assuming a convergence rate of  $\alpha$ , one should have that  $(\text{low} - \text{medium})/(\theta_{lm}^\alpha - 1) = (\text{high} - \text{medium})/(1 - \theta_{hm}^\alpha)$  with  $\theta_{lm} = \Delta_l/\Delta_m$  and  $\theta_{hm} = \Delta_h/\Delta_m$ . The bottom panels show the left and right-hand sides of this equation for the amplitude (left panel) with  $\alpha = 4.0$  and the phase (right panel) with  $\alpha = 3.97$ . This is consistent with the 4-th order convergence expected from the order of discretization and temporal updating in the code.

## 4. Results

A direct comparison of waveforms from the start time of the simulations could introduce spurious nonphysical differences due to gauge effects. All the simulations in our study



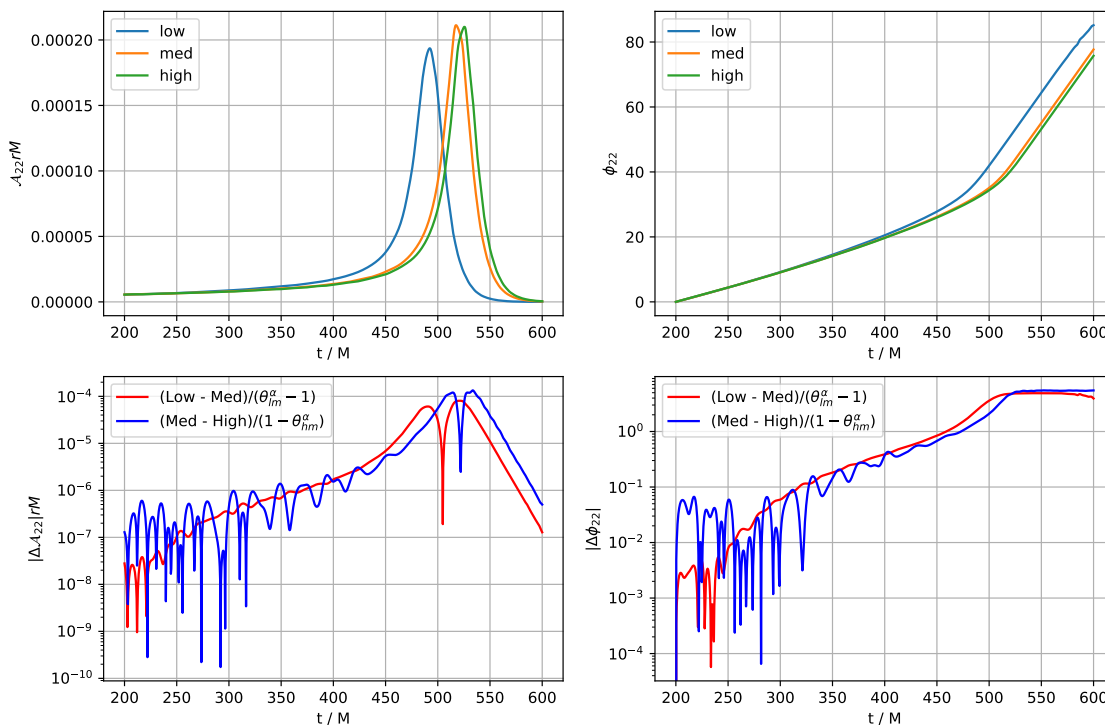


Figure 2: Convergence results for the (2,2) mode of the Weyl Scalar  $\Psi_4$  for mass ratio  $q = 5$  and compactness  $C = 0.173$ . The top panels show the amplitude (left) and phase evolution (right) for three simulations with resolutions at the finest level of  $\Delta_h = 188$  meters (high),  $\Delta_m = 210$  meters (medium), and  $\Delta_l = 339$  meters (low). The bottom panels show the left and right-hand side of equation (low - medium)/ $(\theta_{lm}^\alpha - 1) = (\text{high} - \text{medium})/(1 - \theta_{hm}^\alpha)$  with  $\theta_{lm} = \Delta_l/\Delta_m$  and  $\theta_{hm} = \Delta_h/\Delta_m$ . In the bottom left for the amplitude we used  $\alpha = 4.0$  and in the bottom right panel for the phase  $\alpha = 3.97$ .

were done using the moving puncture gauge, but this does not necessarily imply that the time coordinate in the simulations are *aligned*. This is because of the differences in the parameters of the binaries. This can be seen in Figure 3 where we plot the frequency of the GW as a function of simulation time. Solid lines are polynomial fits to the frequencies from the simulations after the junk radiation has passed [43], approximately at  $140 M$  from the beginning of the simulation. The lines end at  $100 M$  before the merger. The dashed lines are extrapolations back in time. We follow the suggestion in Ref. [15] and shift the time coordinate in the simulation results such that  $t = 0 M$  is the time at which the GW has a specified frequency. We picked this frequency to be  $0.06 M^{-1}$ .

#### 4.1. Inspiral and Tidal Disruption

Figures 4 and 5 show snapshots of the rest mass density in the equatorial plane for two cases with  $q = 3$  and another two for  $q = 5$ , respectively. The top panels in Fig. 4 show



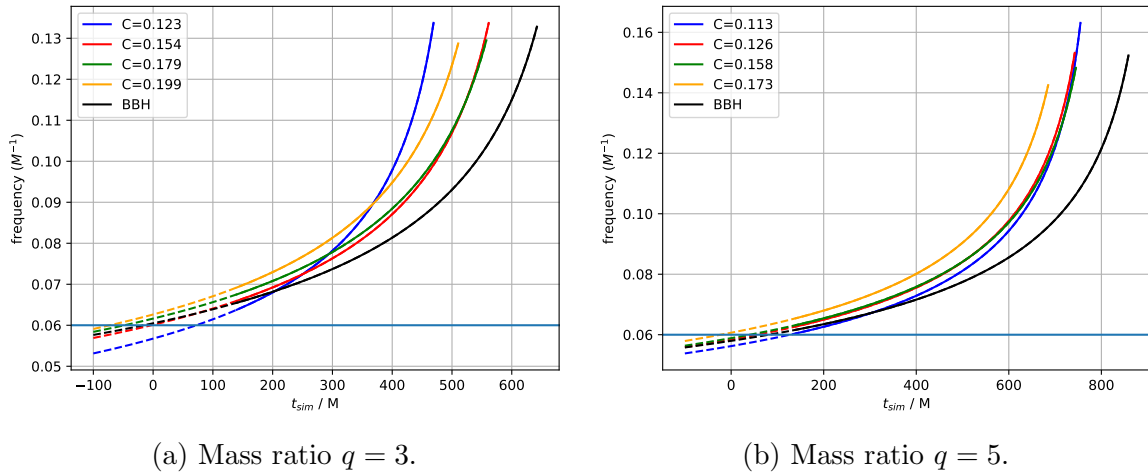


Figure 3: Frequency of the GW as a function of simulation time. Solid lines are polynomial fits to the frequencies from the simulations after the junk radiation has passed, approximately at  $140 M$  from the beginning of the simulation. The lines end at  $100 M$  before the merger. The dashed lines are extrapolations back in time.

the least compact case with  $C = 0.123$  and the bottom panels for the most compact case  $C = 0.199$ . Similarly, the top panels in Fig. 5 show the case  $C = 0.113$  and the bottom panels with  $C = 0.173$ . The white circle denotes the black hole’s apparent horizon in all snapshots.

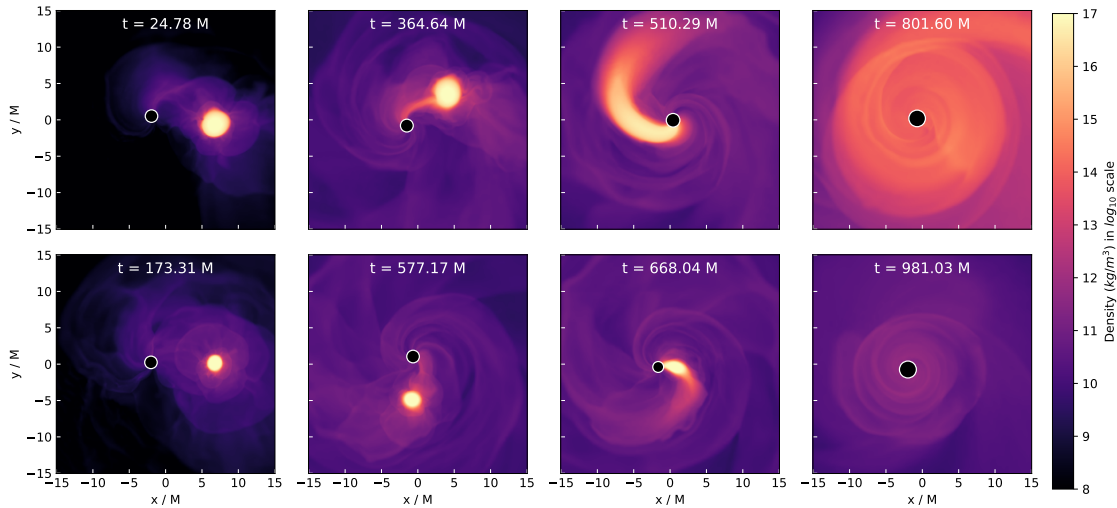


Figure 4: Rest mass density contour snapshots in the equatorial plane for two cases with mass ratio  $q = 3$ . The top panel shows the case  $C = 0.123$ , and the bottom panels are for  $C = 0.199$ . The white circle denotes the black hole’s apparent horizon.

The first thing to notice in Figs. 4 and 5 is that, when comparing the panels for the high compactness cases (bottom panels) between  $q = 3$  and  $q = 5$ , they show very similar qualitatively features. In both cases, the NS is swallowed by the BH, experiencing

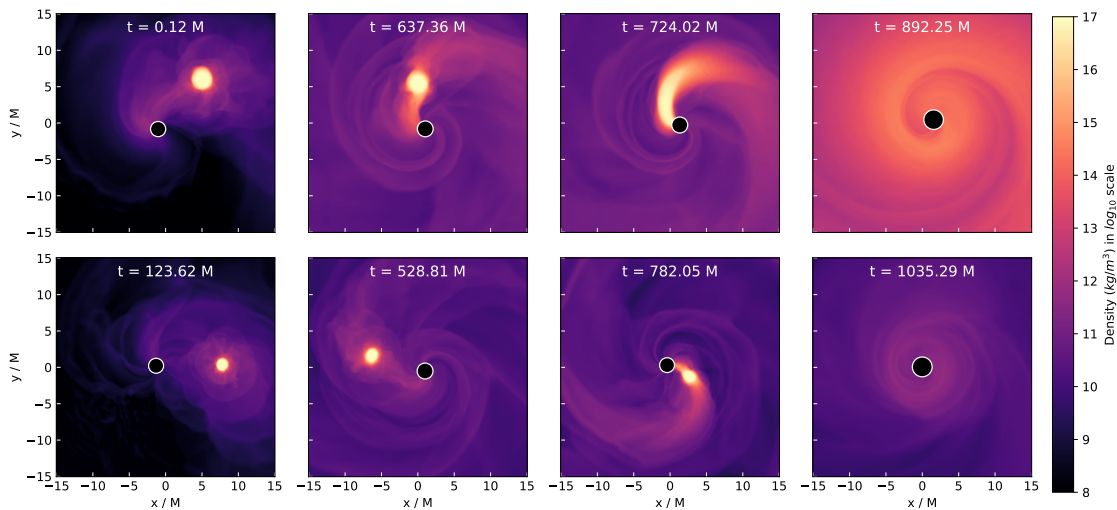


Figure 5: Rest mass density contour snapshots in the equatorial plane for two cases with mass ratio  $q = 5$ . The top panel shows the case  $C = 0.113$ , and the bottom panels are for  $C = 0.173$ . The white circle denotes the black hole’s apparent horizon.

small disruption and mass loss. However, if one pays attention to the time stamp in the snapshots, one sees that the features in the  $q = 5$  case develop later. This is because the energy emitted in GW scales roughly as  $q^2/(1+q)^4$ , and thus the luminosity of the  $q = 3$  case is larger than in  $q = 5$ , i.e., the  $q = 5$  binary merges later.

The low compactness cases also show similar qualitative features and a time delay in  $q = 5$  compared to  $q = 3$ . Here, there is an additional factor besides the one mentioned before depending on  $q$ . The tidal radius scales with compactness and mass ratio as  $r_t \propto C^{-1} q^{-2/3}$ . Thus,  $r_t$  in the case  $q = 5$  is smaller than for  $q = 3$ , and the star is able to inspiral longer before tidal forces from the hole disrupt the star. Nonetheless, before disrupting, the star remains fairly stable, losing less than 0.2% of the initial mass. As the star disrupts, it develops a spiral, fan-looking shape, a tail characteristic of tidal disruptions. The last two snapshots in the top panels of the figures show the late stage. In them, one can observe that as the tidal debris circularizes, there are hints of an accretion disk. The accretion in this stage will have, as we will discuss in a subsequent section, a profound effect on the quasi-normal ringing of the BH.

Finally, we observe that as the compactness increases, the mass shedding of the star and formation of the tidal tail occurs closer to the merger, as expected. This is consistent with the results from the study of quasi-equilibrium states of mixed binaries [14] in which it was found that frequency when shedding initiates is  $\propto C^{3/2}(1+1/q)^{1/2}$ .

#### 4.2. Gravitational waves

Next, we discuss the GW signatures. Figures 6 and 7 show respectively comparisons of the real part of the (2,2) and (3,3) modes of the  $\Psi_4$  Weyl scalar between BBH and NSBH simulations. Panels from top to bottom are arranged in order of increasing compactness.

The figures only show the waveforms after the passing of the junk radiation. It is evident from the retarded time  $T_{mx}$  when the amplitude of  $\Psi_4$  reaches its maximum that NSBH binaries merge earlier than the corresponding mass ratio BBHs (for specific values of  $T_{mx}$  in the (2,2) mode see Table 2). This is expected as stellar deformation leads to an additional correction term in the gravitational potential, which accelerates the mergers by larger dissipation of GWs [13]. The same comparison with similar characteristics but for the  $q = 5$  case is depicted in Figs. 8 and 9. We observe the trend that merger occurs later as compactness increases. This is expected since, as mentioned before, the NSBH binary behaves closer to a BBH as compactness increases. At the same time, the time to reach peak amplitude  $T_{mx}$  is larger since these  $q = 5$  binaries are not as luminous as the  $q = 3$ . An interesting observed feature is that the monotonic dependence of  $T_{mx}$  with compactness  $C$  in  $q = 5$  does not translate into the  $q = 3$ . The NSBH with  $C = 0.199$  seems to merge earlier than the  $C = 0.179$  (see Table 4). We have not found a reason for this behavior.

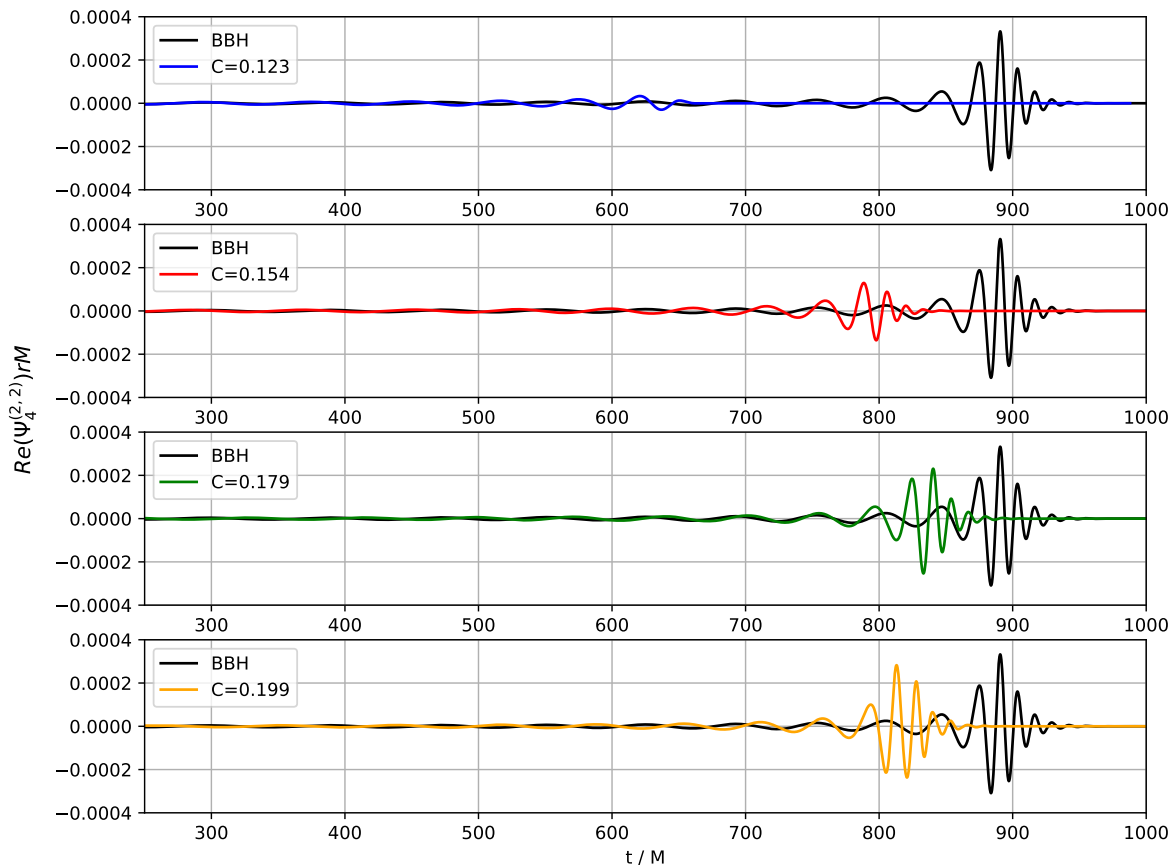


Figure 6: Comparison of  $Re(\Psi_4^{(2,2)})rM$  for the  $q = 3$  case between BBH and NSBH simulations. Panels from top to bottom are in increasing compactness cases.

Another way of analyzing the differences in the waveforms is by looking separately at the amplitude and phase for the (2,2) mode of  $\Psi_4$ . Figure 10 depicts the amplitude (left panels) and phase (right panels) of  $\Psi_4$  for  $q = 3$  (top panels) and  $q = 5$  (bottom

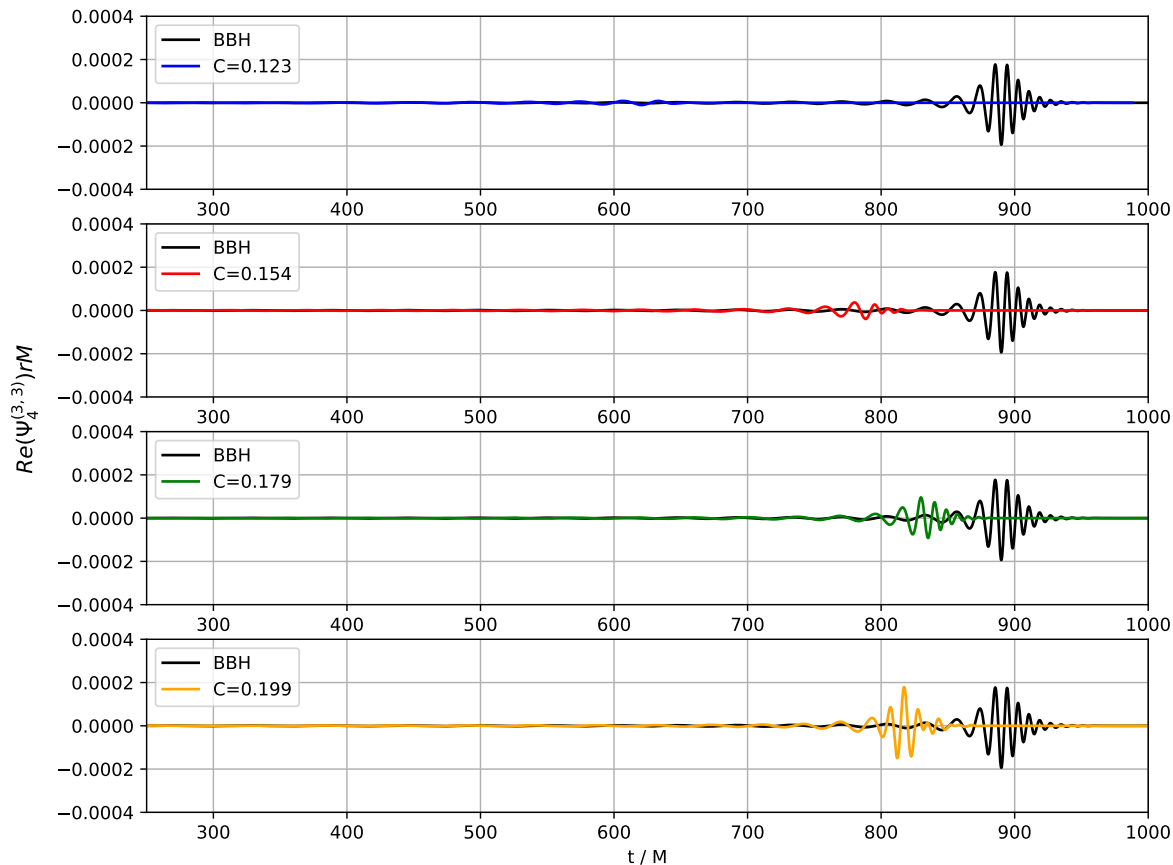
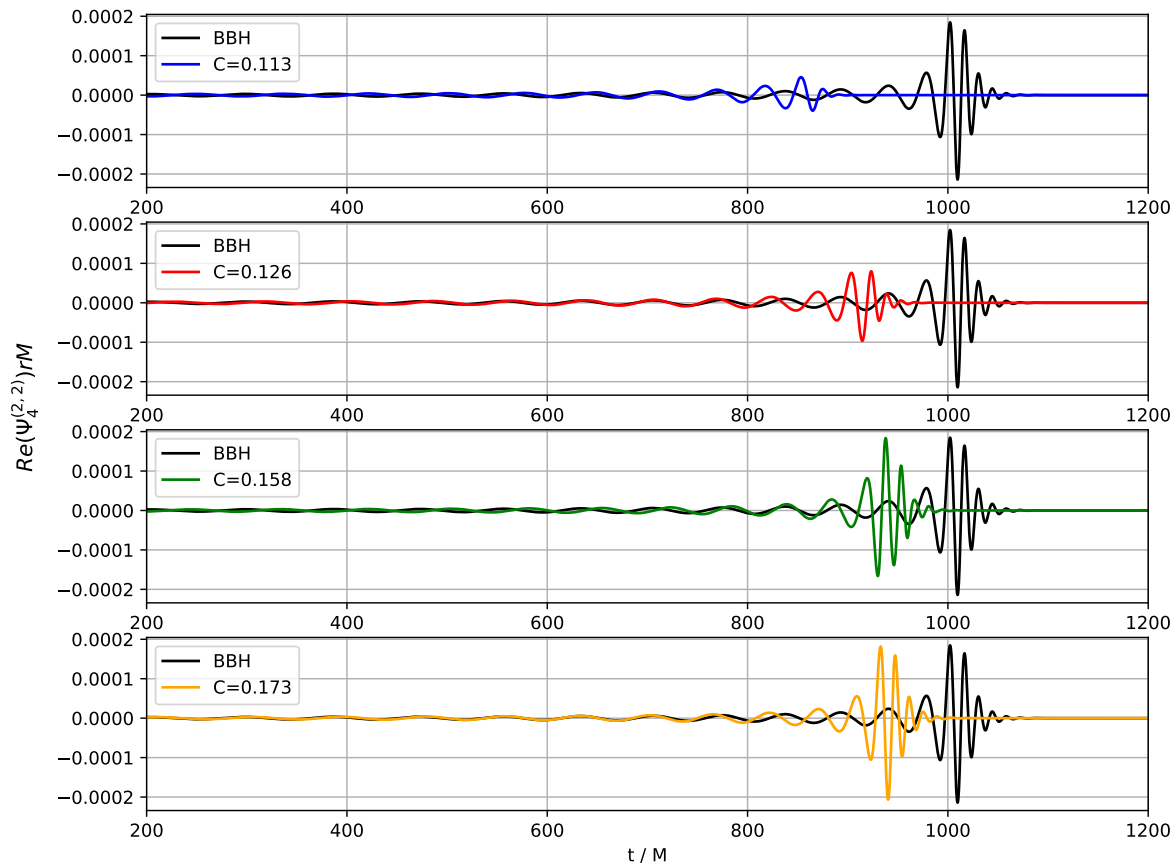


Figure 7: Same as in Fig. 6 but for the mode  $Re(\Psi_4^{(3,3)})$ .

panels) cases. The amplitudes have been shifted in time to agree at peak. The time shifts are the merger times given in Table 2 added with  $130 M$  for radiation to propagate. The same time shift was applied to the phase plus a phase shift, so the phases align at peak amplitude. The amplitude of  $\Psi_4$  increases monotonically with compactness but remains smaller than in the BBH case. This is consistent with NSBH binaries radiating less energy and angular momentum, as we shall see in Sec 4.5 in Table 4.

$q = 3$		$q = 5$	
$C$	$T_{mx}/M$	$C$	$T_{mx}/M$
BBH	758	BBH	877
0.123	497	0.113	727
0.154	664	0.126	785
0.179	705	0.158	804
0.199	683	0.173	807

Table 2:  $T_{mx}$  is the retarded time at which the amplitude of the (2,2) mode of  $\Psi_4$  reaches a maximum with an extraction radius of  $130 M$ .


 Figure 8: Same as in Fig. 6 but for the case  $q = 5$ .

### 4.3. Spectra and Mismatches

It is important to investigate also the differences and similarities in the waveforms with the framework commonly used in GW data analysis. We follow the procedures in Ref. [44] and use the data analysis tool from LSC Algorithm Library [45]. First, we compute the spectrum of the characteristic strain  $h_c(f) = 2f|\tilde{h}(f)|$ , with  $|\tilde{h}(f)|^2 = (|\tilde{h}_+(f)|^2 + |\tilde{h}_\times(f)|^2)/2$ . Here,  $\tilde{h}_+(f)$  and  $\tilde{h}_\times(f)$  are the Fourier transform of the plus and cross-polarization of the strain at a distance of 150 Mpc, calculated from  $\Psi_4$  including up to the  $l = 8$  mode. Figure 11 shows the spectrum of  $h_c$  for all compactness cases under consideration and for a BBH (left panel for  $q = 3$  and right panel for  $q = 5$ ). The figures include the sensitivity curves for LIGO (obtained from LSC Algorithm Library for second-generation detectors) and the Einstein Telescope. Not surprisingly, the larger the compactness, the closer the spectrum for  $h_c$  is to the BBH case.

Next, we calculate mismatches between the strains from NSBH binaries and the one from a BBH. The mismatches are computed from  $1 - \mathcal{O}(h_1|h_2)$ , with the match or overlap given by

$$\mathcal{O}(h_1|h_2) = \frac{\max_{\phi_c, t_c} \langle h_1|h_2 \rangle}{\sqrt{\langle h_1|h_1 \rangle \langle h_2|h_2 \rangle}} \quad (25)$$

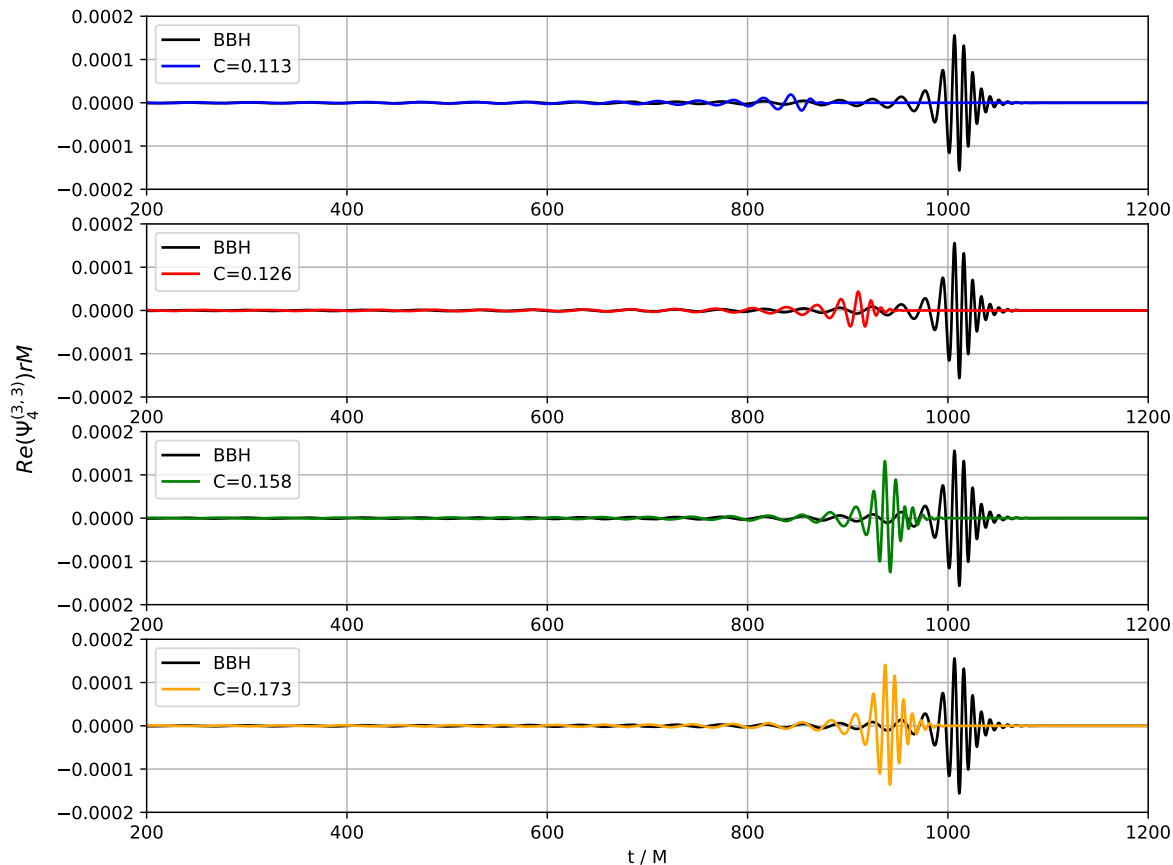


Figure 9: Same as in Fig. 8 but the mode  $Re(\Psi_4^{(3,3)})$ .

where

$$\langle h_1 | h_2 \rangle \equiv 4\text{Re} \int_{f_{mn}}^{f_{mx}} \frac{\tilde{h}_1^*(f) \tilde{h}_2(f)}{S_n(f)} df. \quad (26)$$

The maximization is over coalescence time  $t_c$  and coalescence phase  $\phi_c$ . In Eq. (26),  $S_n$  is the one-sided power spectral density (sensitivity curve) of the detector noise. We considered sensitivity curves for LIGO and the Einstein Telescope (ET).

Table 3 shows the mismatches of the plus polarization  $h_+$  for  $q = 3$  and 5 at inclination angles  $\iota = 0, \pi/6$ , and  $\pi/3$ . To eliminate errors due to Gibbs phenomena when taking the FFTs, we taper the first 3 cycles of the waveform and start the integration in Eq. (26) at  $f_{mn}$ . The upper limit of integration is set to  $f_{mx}$  to cover the merger as shown in Fig. 11 in the shaded area. The integration range for  $q = 3$  is  $[f_{mn}, f_{mx}] = [320, 4096]\text{Hz}$ , and for  $q = 5$ ,  $[f_{mn}, f_{mx}] = [550, 4096]\text{Hz}$ . These bounds of integration are set to ensure a fair comparison between mismatches across cases with different compactness, detectors, and inclination angles.

For a given mass ratio and inclination, the mismatches decrease with increasing compactness since, as mentioned before, an increase in compactness brings the NSBH binary to look more like a BBH. The exception is the  $q = 3, C = 0.199$  case. Its mismatches are larger than for  $q = 3, C = 0.179$ . This is connected to the observation

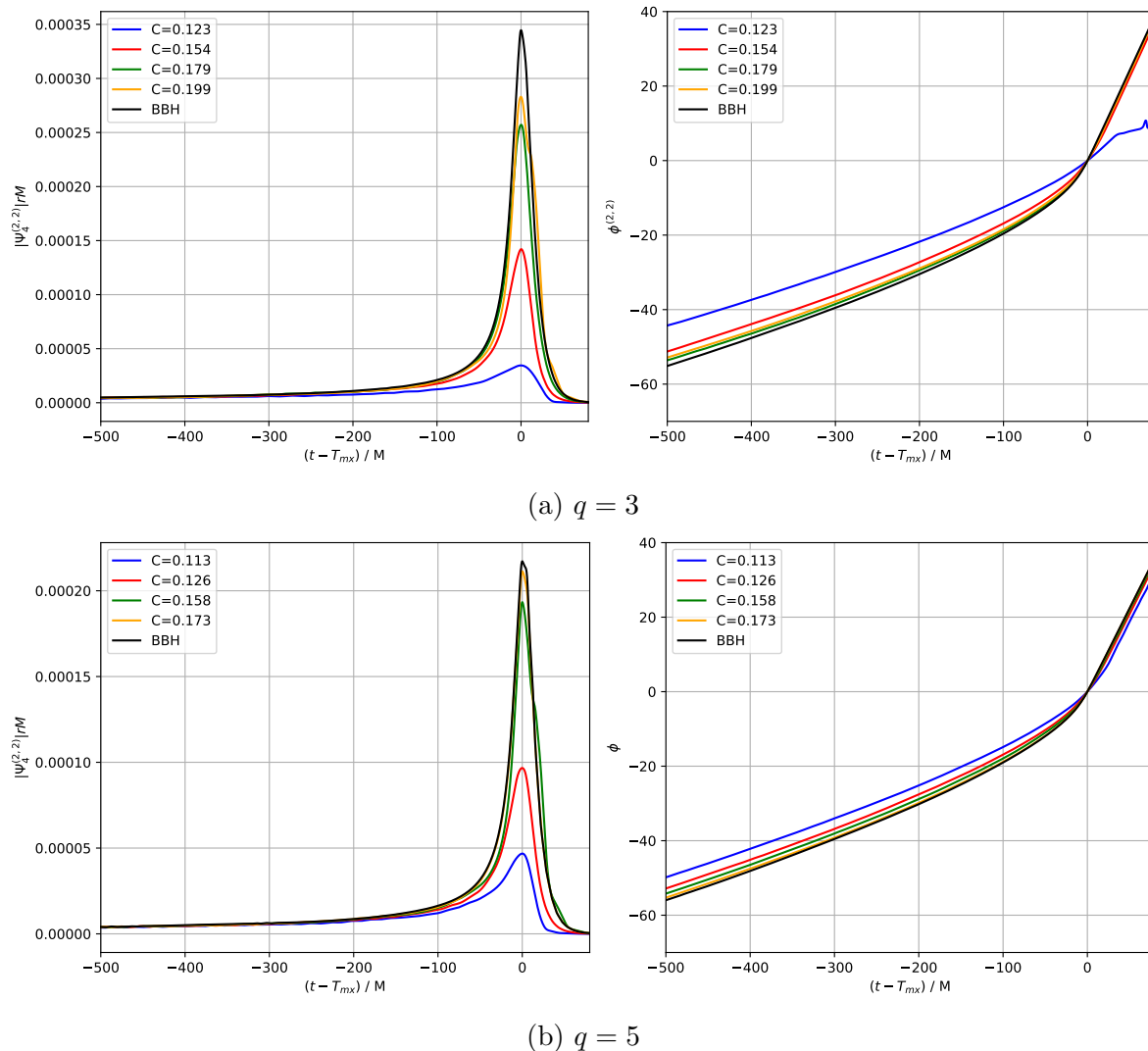


Figure 10: Amplitude (left panels) and phase (right panels) of the (2,2) mode of  $\Psi_4$  for the  $q = 3$  (top panels) and  $q = 5$  (bottom panels). Amplitude comparison between BBH and NSBH configurations. The amplitudes have been shifted in time to agree at peak. The same time shift was applied to the phase plus a phase shift, so the phase align at peak amplitude.

made in Sec. 4.2 that the  $q = 3$ ,  $C = 0.199$  NSBH binary merges earlier than the  $q = 3$ ,  $C = 0.179$  binary. Finally, as the inclination angle increases, the mismatch increases accordingly. For  $\iota = \pi/3$ , mismatches for mass ratio  $q = 3$  can go up 0.07 – 0.15 while  $q = 5$  mismatches go up to 0.01 – 0.14. This indicates that the inclusion of higher-order modes reveals more information to distinguish between NSBH and BBH waveforms [12]. The standard mismatch cutoff for LIGO sensitivity to claim two waveforms are similar enough is  $\lesssim 0.02$ . Thus, from the results in Table 3, only the  $C = 0.173$ ,  $q = 5$  is “indistinguishable” from a BBH independently of the inclination angle. This is consistent with what we have been pointing out several times that this case is the



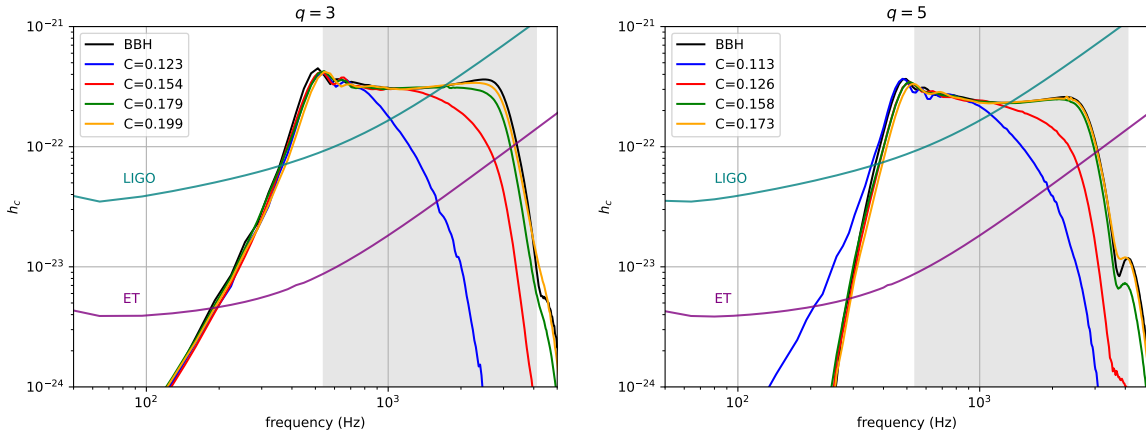


Figure 11: Fourier spectrum of the characteristic strain  $h_c$  for mass ratio  $q = 3$  (left) and  $q = 5$  (right), on top of the sensitivity curves for LIGO and ET.

		$q = 3$					
		$\iota = 0$		$\iota = \pi/6$		$\iota = \pi/3$	
$C$		LIGO	ET	LIGO	ET	LIGO	ET
0.123		0.0796	0.0844	0.1071	0.1116	0.1490	0.1537
0.154		0.0123	0.0125	0.0371	0.0376	0.0845	0.0856
0.179		0.0080	0.0080	0.0371	0.0377	0.0922	0.0940
0.199		0.0104	0.0102	0.0346	0.0347	0.0739	0.0746
		$q = 5$					
		$\iota = 0$		$\iota = \pi/6$		$\iota = \pi/3$	
$C$		LIGO	ET	LIGO	ET	LIGO	ET
0.113		0.0350	0.0391	0.0667	0.0739	0.1239	0.1372
0.126		0.0107	0.0115	0.0431	0.0480	0.1094	0.1209
0.158		0.0040	0.0040	0.0326	0.0361	0.0957	0.1061
0.173		0.0076	0.0073	0.0073	0.0074	0.0118	0.0120

Table 3: Mismatches between the NSBH waveforms and the waveform of a BBH for three inclination angle  $\iota$  and sensitivity curves for LIGO and the Einstein Telescope.

one that behaves closer to a BBH. If we focus on zero inclination angle, some cases with lower compactness have mismatches  $< 0.02$ , thus also “indistinguishable.”

#### 4.4. Impact of the spurious neutron star oscillation

As pointed out in our previous study [12], our framework to construct initial data triggers spurious breathing modes in the NS. Figure 12 shows the oscillations in the central density of the star due to the “imperfections” in the initial data. The left panels

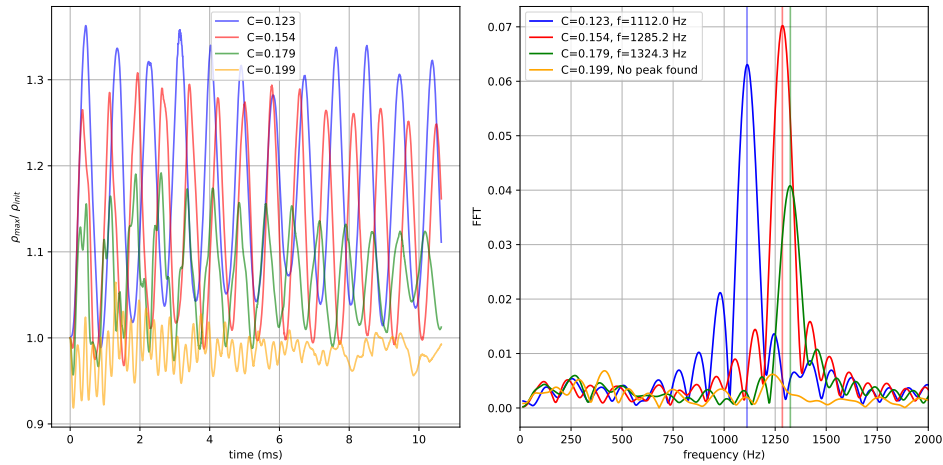
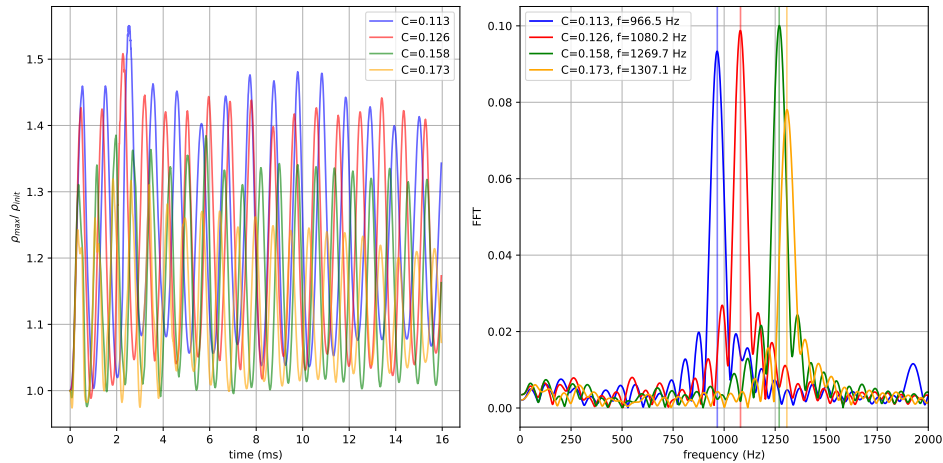

 (a)  $q = 3$ 

 (b)  $q = 5$ 

Figure 12: The left panels show the oscillations in the central density of the NS normalized to the initial central density of the star. The right panels show the corresponding FFT, with the insert showing the peak frequency. No significant peak was found for the case  $C = 0.199$ ,  $q = 3$ .

show the oscillations relative to the initial central density, and the corresponding right panels show the Fourier transforms. Two interesting observations can be made here. First, smaller stars (higher compactness) exhibit smaller amplitude oscillations, while larger stars (lower compactness) can have oscillations in the central density, reaching amplitudes of  $\sim 25\%$  of its initial value. The observed oscillations are a manifestation of radial oscillation in the NS [46] triggered by the initial data setup. Since they are radial oscillations, they do not leave an imprint in the GWs emitted.

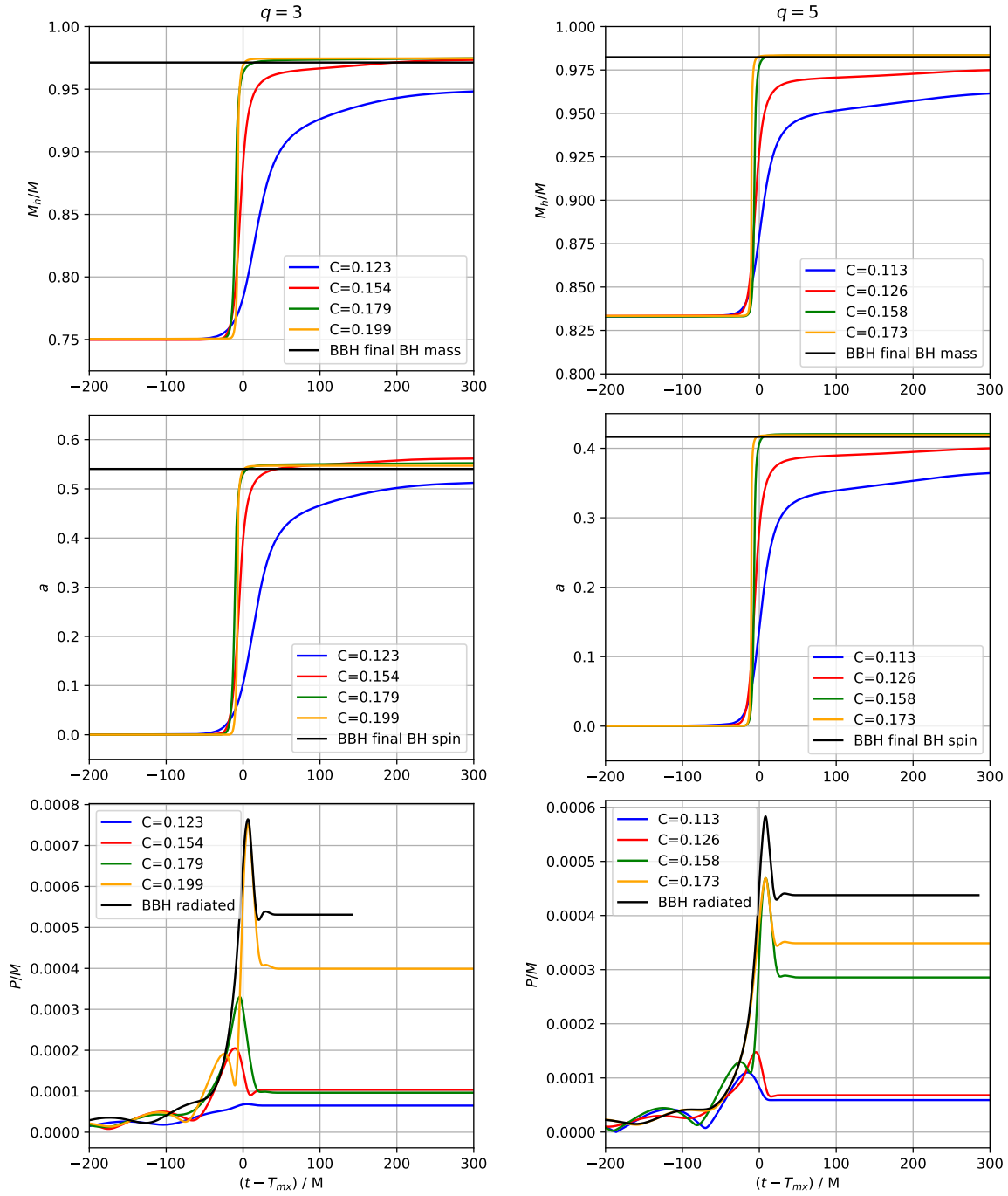


Figure 13: From top to bottom, the mass and spin of the BH and the radiated linear momentum during the course of the simulation. The left panels are for the  $q = 3$  and the right for  $q = 5$ . For the mass and spin, the black lines denote the value of the mass and spin for the final BH in the BBH merger. The black lines in the bottom panels are the evolution of the radiated linear momentum for the BBH system. Time for each case has been shifted to align when  $\Psi_4^{(2,2)}$  reaches peak amplitude.

#### 4.5. The Final State

Figure 13 shows, from top to bottom, the mass and spin of the BH and the radiated linear momentum during the course of the simulation. The left panels are for the  $q = 3$  and the right for  $q = 5$ . For the mass and spin, the black lines denote the value of the mass and spin for the final BH in the BBH merger. The black lines in the bottom panels are the evolution of the radiated linear momentum for the BBH system. Time for each case has been shifted to align when  $\Psi_4^{(2,2)}$  reaches peak amplitude. The mass and spin of the BH after the merger increase with the compactness of the star. The lower the compactness of the NS, the slower the growth of the mass and spin of final BH. This is because the BH takes longer to accrete the debris from the disrupted NS. In the extreme cases where the NSs have the lowest compactness,  $C = 0.123$  and  $0.113$ , the mass and spin of the final BH are significantly lower than the corresponding mass and spin of the final BH from a BBH merger. In these cases, between 15% and 10% of the mass and angular momentum of the NS remains trapped in the accretion disk surrounding the BH still present at the end of the simulation.

$C$	$M_T/M$	$M_h/M$	$M_{ej}/M$	$E_{rad}/M$	$J_T/M^2$	$a$	$J_{rad}/M^2$	$v_k(km/s)$
$q = 3$								
BBH	0.9918	0.9713	0.00	0.0205	0.7025	0.5405	0.1926	163.93
0.123	0.9644	0.9515	8.49e-03	0.0044	0.5531	0.5182	0.0839	20.48
0.154	0.9854	0.9736	1.78e-03	0.0100	0.6670	0.5620	0.1343	31.95
0.179	0.9915	0.9747	1.33e-03	0.0155	0.6882	0.5523	0.1634	29.59
0.199	0.9926	0.9746	1.55e-05	0.0180	0.6921	0.5470	0.1724	122.76
$q = 5$								
BBH	0.9940	0.9824	0.00	0.0116	0.5231	0.4165	0.1212	133.54
0.113	0.9728	0.9624	6.16e-03	0.0042	0.4134	0.3665	0.0739	18.41
0.126	0.9888	0.9754	7.17e-03	0.0062	0.4698	0.4011	0.0881	20.91
0.158	0.9936	0.9834	2.11e-05	0.0102	0.5171	0.4206	0.1103	87.07
0.173	0.9944	0.9834	1.48e-04	0.0108	0.5159	0.4189	0.1107	106.31

Table 4: Final properties of the mergers.  $M_T = M_h + M_{ej} + E_{rad}$  with  $M_h$  the mass of the final BH computed from the Christodoulou mass,  $M_{ej}$  the mass ejected beyond a radius  $35M$  from the binary, and  $E_{rad}$  the energy radiated in GWs.  $J_T/M^2 = a(M_h/M)^2 + J_{rad}/M^2$ , with  $a$  the dimensionless spin of the final BH and  $J_{rad}$  the angular momentum radiated in GWs.  $v_k$  is the kick of the final BH. For reference,  $E_{ADM}/M = 0.9917$  ( $q = 3$ ),  $E_{ADM}/M = 0.994$  ( $q = 5$ ),  $J_{ADM}/M^2 = 0.7023$  ( $q = 3$ ), and  $J_{ADM}/M^2 = 0.523$  ( $q = 5$ ) at the start of the simulation.

Table 4 shows the final properties of the mergers.  $M_T = M_h + M_{ej} + E_{rad}$  is the total mass-energy at the end of the simulation, with  $M_h$  the mass of the final BH

computed from the Christodoulou mass,  $M_{ej}$  the mass ejected beyond a radius  $35 M$  from the binary, and  $E_{rad}$  the energy radiated in GWs.  $J_T/M^2 = a(M_h/M)^2 + J_{rad}/M^2$  is the total angular momentum with  $a$  the dimensionless spin of the final BH and  $J_{rad}$  the angular momentum radiated in GWs.  $v_k$  is the kick of the final BH. For reference, the initial energy and angular momentum are  $E_{ADM}/M = 0.9917$  ( $q = 3$ ),  $E_{ADM}/M = 0.994$  ( $q = 5$ ),  $J_{ADM}/M^2 = 0.7023$  ( $q = 3$ ), and  $J_{ADM}/M^2 = 0.523$  ( $q = 5$ ) at the start of the simulation.

In the highest compactness cases,  $M_T/M$  exceeds  $M_{ADM}/M$ . This is because of the inaccuracy of calculating  $E_{rad}/M$  at a finite distance from the binary. On the other hand, for low compactness,  $J_T/M^2$  is significantly smaller than  $J_{ADM}/M^2$  because of the material that is not accounted for within the radius where the ejected material is calculated.

From  $E_{rad}$  and  $J_{rad}$  in Table 4, we observe that the BBH system is the one that produced the largest radiation. In contrast, the NSBH systems produce smaller radiation emission, but it grows monotonically with the compactness. There are two main reasons for this. Low compactness yields disruption, which damps GW emission. The other reason is, as mentioned before, low compactness accelerates the merger and, thus, restrains the total amount of emitted radiation.

#### 4.6. Quasi-normal ringing

Figures 14 and 15 show the post-merger  $\Psi_4$  signal for  $q = 3$  and 5, respectively. The left panels depict the amplitude of  $\Psi_4$  for the modes (2,1), (2,2), and (3,3), with the right panels showing their phases. The times have been shifted so amplitude and phase align at peak luminosity. Given the masses and spins of the final BH from Table 4, the top half in Tables 5 and 6 show the quasi-normal mode (QNM) frequencies  $\omega$  and damping times  $\tau$  for each mode from Ref. [47]. The bottom half of these tables shows the QNM values for  $\omega$  and  $\tau$  from fittings of  $\Psi_4 \propto \exp(-t/\tau) \sin(\omega t)$  to our simulation data. For low compactness, the signal does not exhibit a *clean* QNM ringing. This is because the BH is accreting tidal debris. The oscillations observed in the amplitude for high compactness are due to mode mixing in our extraction procedure.

## 5. Conclusions

The present study investigated the effect of varying the compactness of the NS on NSBH mergers with polytropic EOS. We considered four compactness cases for mass ratios  $q = 3$  and 5 to compare the inspiral and merger dynamics, the GWs emitted, the properties of the final BH, including its QNM ringing. The NSBH system behaves more and more like a BBH as the compactness increases. For low compactness, the tidal debris resembles an accretion, and the GW signal is dramatically different from that of a BBH with the same mass ratio. The compactness also affects the merger time. For low compactness, the binary merges  $100 - 200 M$  earlier than then BBH. The QNM

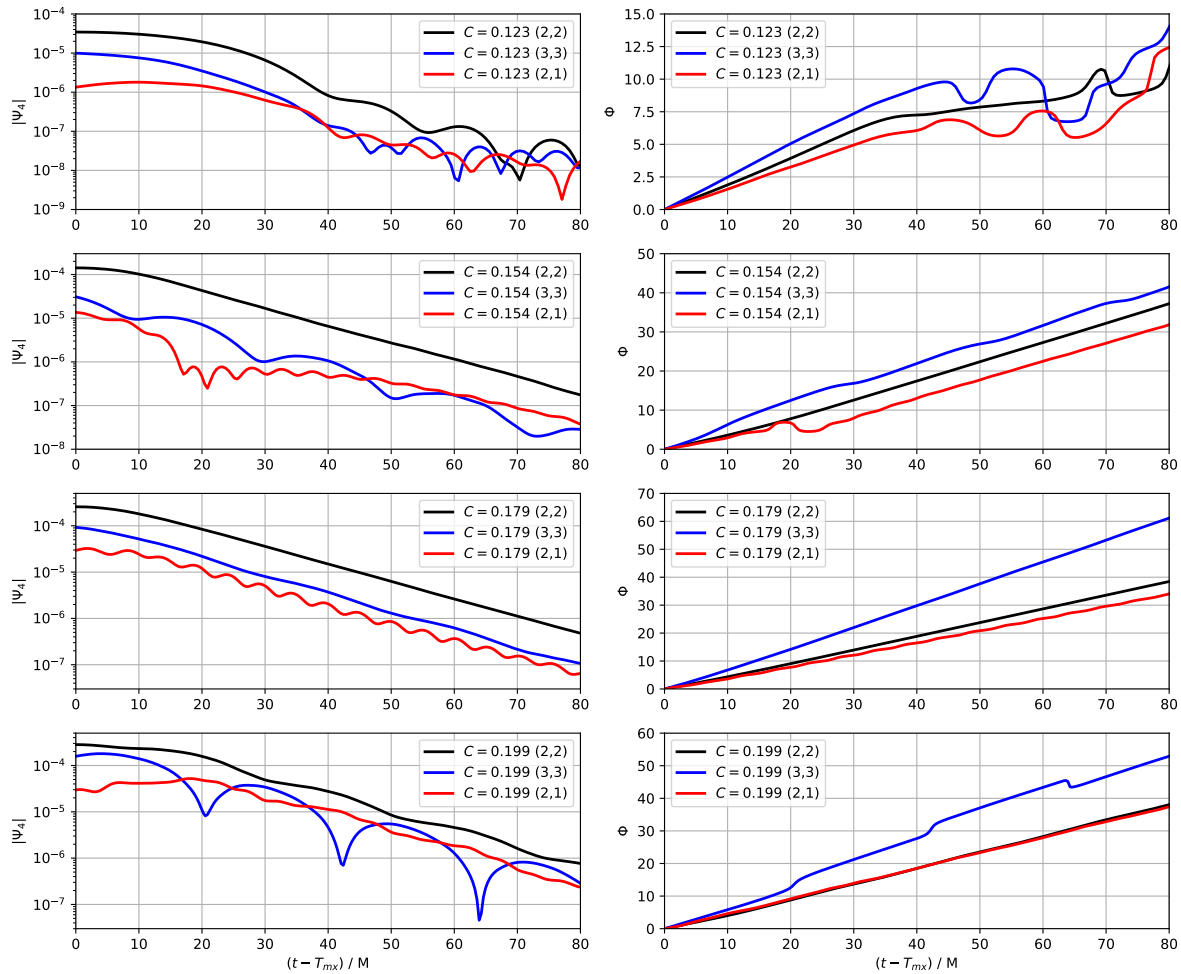
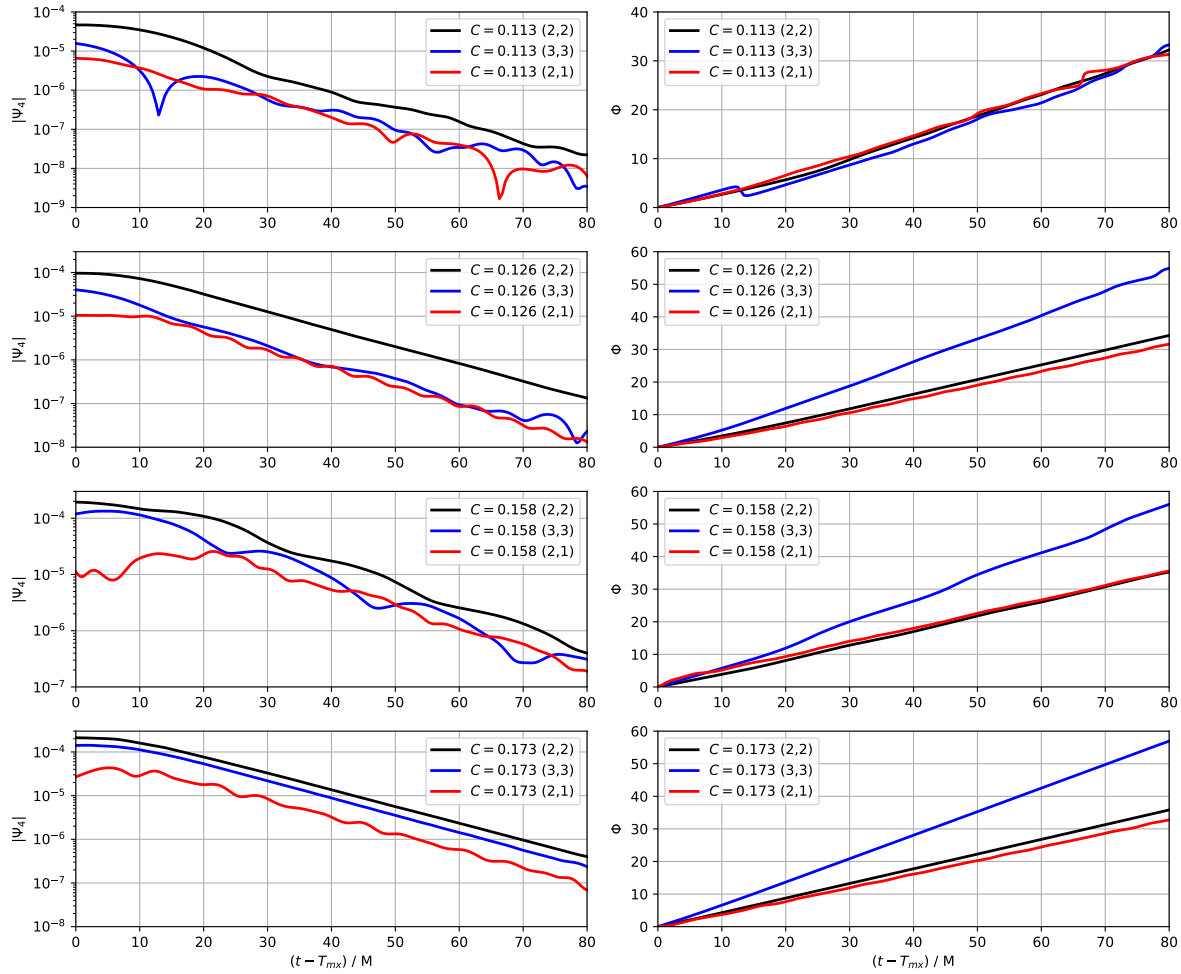


Figure 14: Post-merger  $\Psi_4$  signal for  $q = 3$ . The left panels depict the amplitude of  $\Psi_4$  for the modes (2,1), (2,2), and (3,3), with the right panels showing their phases. The times have been shifted so amplitude and phase align at peak luminosity.

ringing of the final BH was significantly affected by the effects of tidal disruption. Clean QNM modes are only observed for high compactness cases. For low compactness, the tidal debris accreting into the final BH contaminates the signal. Mismatches between NSBH and BBH waveforms showed that the mismatches decrease for higher compactness cases, while the inclusion of higher-order modes for larger inclination angles leads to higher mismatches. When put together, the QNM and mismatches results, NSBH with low compactness are the best candidates to investigate the signatures from NSBH coalescences.

*Acknowledgements* This work is supported by NSF grants PHY-2114582 and PHY-2207780. We would like to thank Kostas Kokkotas, Deborah Ferguson, Deirdre Shoemaker, Aasim Jan, and Francois Foucart for insightful discussions and for sharing their resources for this work.


 Figure 15: Same as in Fig. 14 but for  $q = 5$ .

- [1] Abbott R et al. (LIGO Scientific Collaboration, Virgo Collaboration, and KAGRA Collaboration) 2023 Phys. Rev. X **13**(4) 041039 URL <https://link.aps.org/doi/10.1103/PhysRevX.13.041039>
- [2] Shibata M, Kyutoku K, Yamamoto T and Taniguchi K 2009 Phys. Rev. D **79**(4) 044030 URL <http://link.aps.org/doi/10.1103/PhysRevD.79.044030>
- [3] Duez M D, Foucart F, Kidder L E, Ott C D and Teukolsky S A 2010 Classical and Quantum Gravity **27** 114106–+ (*Preprint* 0912.3528)
- [4] Kyutoku K, Shibata M and Taniguchi K 2010 Phys. Rev. D **82** 044049 [Erratum: Phys.Rev.D 84, 049902 (2011)] (*Preprint* 1008.1460)
- [5] Read J S, Markakis C, Shibata M, Uryū K b o, Creighton J D E and Friedman J L 2009 Phys. Rev. D **79**(12) 124033 URL <https://link.aps.org/doi/10.1103/PhysRevD.79.124033>
- [6] Kyutoku K, Okawa H, Shibata M and Taniguchi K 2011 Phys. Rev. D **84** 064018 (*Preprint* 1108.1189)
- [7] Etienne Z B, Liu Y T, Shapiro S L and Baumgarte T W 2009 Phys. Rev. D **79**(4) 044024 URL <https://link.aps.org/doi/10.1103/PhysRevD.79.044024>
- [8] Foucart F, Duez M D, Kidder L E and Teukolsky S A 2011 Phys. Rev. D **83**(2) 024005 URL <http://link.aps.org/doi/10.1103/PhysRevD.83.024005>
- [9] Etienne Z B, Liu Y T, Paschalidis V and Shapiro S L 2012 Phys. Rev. D **85**(6) 064029 URL <https://link.aps.org/doi/10.1103/PhysRevD.85.064029>



$C$	$\omega_{(2,1)}$	$\tau_{(2,1)}$	$\omega_{(2,2)}$	$\tau_{(2,2)}$	$\omega_{(3,3)}$	$\tau_{(3,3)}$
From Ref. [47]						
0.123	0.445	11.639	0.493	11.726	0.787	11.326
0.154	0.442	11.738	0.496	11.839	0.790	11.462
0.179	0.440	11.716	0.492	11.814	0.784	11.431
0.199	0.439	11.704	0.491	11.800	0.782	11.415
From Simulations						
0.123	0.080	10.622	0.084	8.112	0.077	10.923
0.154	0.472	22.001	0.491	11.085	0.488	10.838
0.179	0.434	11.682	0.491	11.534	0.783	11.181
0.199	0.471	11.288	0.489	11.301	0.653	12.045

Table 5: QNMs frequency  $\omega$  and decaying time scale  $\tau$  in units of the final BH mass  $M_h$  for the most dominant modes for the  $q = 3$  cases. The top half are values from Ref. [47] and the bottom half from fittings to our simulation data.

$C$	$\omega_{(2,1)}$	$\tau_{(2,1)}$	$\omega_{(2,2)}$	$\tau_{(2,2)}$	$\omega_{(3,3)}$	$\tau_{(3,3)}$
From Ref. [47]						
0.113	0.420	11.424	0.450	11.472	0.720	11.042
0.126	0.418	11.456	0.451	11.509	0.722	11.089
0.158	0.418	11.485	0.452	11.544	0.723	11.125
0.173	0.417	11.482	0.452	11.541	0.723	11.122
From Simulations						
0.113	0.429	10.451	0.444	10.091	0.459	10.612
0.126	0.420	10.410	0.449	10.954	0.718	10.705
0.158	0.434	12.312	0.452	11.120	0.724	10.962
0.173	0.417	11.231	0.451	11.345	0.722	11.012

Table 6: Same as in Table 5 but for the  $q = 5$ .

- [10] Etienne Z B, Paschalidis V and Shapiro S L 2012 *Phys. Rev. D* **86**(8) 084026 URL <https://link.aps.org/doi/10.1103/PhysRevD.86.084026>
- [11] Foucart F 2012 *Phys. Rev. D* **86** 124007 (*Preprint* [1207.6304](https://arxiv.org/abs/1207.6304))
- [12] Khamesra B, Gracia-Linares M and Laguna P 2021 *Classical and Quantum Gravity* **38** 185008 URL <https://doi.org/10.1088%2F1361-6382%2Fac1a66>
- [13] Shibata M and Taniguchi K 2011 *Living Rev. Rel.* **14** 6
- [14] Taniguchi K, Baumgarte T W, Faber J A and Shapiro S L 2008 *Phys. Rev. D* **77** 044003 (*Preprint* [0710.5169](https://arxiv.org/abs/0710.5169))
- [15] Foucart F, Buchman L, Duez M D, Grudich M, Kidder L E, MacDonald I, Mroue A, Pfeiffer H P, Scheel M A and Szilagyi B 2013 *Phys. Rev. D* **88** 064017 (*Preprint* [1307.7685](https://arxiv.org/abs/1307.7685))

- [16] Foucart F, Deaton M B, Duez M D, Kidder L E, MacDonald I, Ott C D, Pfeiffer H P, Scheel M A, Szilagyi B and Teukolsky S A 2013 Phys. Rev. D **87**(8) 084006 URL <https://link.aps.org/doi/10.1103/PhysRevD.87.084006>
- [17] Clark M and Laguna P 2016 Phys. Rev. D **94** 064058 (*Preprint* [1606.04881](https://arxiv.org/abs/1606.04881))
- [18] Baumgarte T W and Shapiro S L 2010 Numerical Relativity: Solving Einstein's Equations on the Computer (Cambridge University Press)
- [19] Smarr L L (ed) 1979 Proceedings, Sources of Gravitational Radiation: Seattle, WA, USA, July 24 - August 4, 1978 (Cambridge: Cambridge Univ. Press)
- [20] Bowen J M and York Jr J W 1980 Phys. Rev. D **21** 2047–2056
- [21] Bowen J M 1979 General Relativity and Gravitation **11** 227–231 ISSN 1572-9532 URL <https://doi.org/10.1007/BF00762132>
- [22] Ansorg M, Brüggmann B and Tichy W 2004 Phys. Rev. D **70** 064011
- [23] Evans C, Laguna P and Eracleous M 2015 The Astrophysical Journal Letters **805** L19 ISSN 2041-8205
- [24] Clark M and Laguna P 2016 Physical Review D **94** 064058
- [25] Jani K, Healy J, Clark J A, London L, Laguna P and Shoemaker D 2016 Classical and Quantum Gravity **33** 204001 ISSN 0264-9381
- [26] Cupp S et al. 2023 The einstein toolkit URL <https://doi.org/10.5281/zenodo.10380404>
- [27] Baumgarte T W and Shapiro S L 1998 Phys. Rev. D **59**(2) 024007 URL <https://link.aps.org/doi/10.1103/PhysRevD.59.024007>
- [28] Shibata M and Nakamura T 1995 Phys. Rev. D **52**(10) 5428–5444 URL <https://link.aps.org/doi/10.1103/PhysRevD.52.5428>
- [29] Beyer H R and Sarbach O 2004 Phys. Rev. D **70** 104004 (*Preprint* [gr-qc/0406003](https://arxiv.org/abs/gr-qc/0406003))
- [30] Baiotti L, Hawke I, Montero P J, Löffler F, Rezzolla L, Stergioulas N, Font J A and Seidel E 2005 Phys. Rev. D **71** 024035 (*Preprint* [gr-qc/0403029](https://arxiv.org/abs/gr-qc/0403029))
- [31] Hawke I, Löffler F and Nerozzi A 2005 Phys. Rev. D **71** 104006 (*Preprint* [gr-qc/0501054](https://arxiv.org/abs/gr-qc/0501054))
- [32] Baiotti L, Hawke I, Montero P J and Rezzolla L 2003 Mem. Soc. Ast. It. **1** S210 (*Preprint* [1004.3849](https://arxiv.org/abs/1004.3849))
- [33] Campanelli M, Lousto C, Marronetti P and Zlochower Y 2006 Phys. Rev. Lett. **96** 111101 (*Preprint* [gr-qc/0511048](https://arxiv.org/abs/gr-qc/0511048))
- [34] Baker J G, Centrella J, Choi D I, Koppitz M and van Meter J 2006 Phys. Rev. Lett. **96** 111102 (*Preprint* [gr-qc/0511103](https://arxiv.org/abs/gr-qc/0511103))
- [35] Thornburg J 2004 Class. Quant. Grav. **21** 743–766 (*Preprint* [gr-qc/0306056](https://arxiv.org/abs/gr-qc/0306056))
- [36] Löffler F et al. 2012 Class. Quant. Grav. **29** 115001 (*Preprint* [1111.3344](https://arxiv.org/abs/1111.3344))
- [37] Ashtekar A and Krishnan B 2004 Living Reviews in Relativity **7** 10 (*Preprint* [gr-qc/0407042](https://arxiv.org/abs/gr-qc/0407042))
- [38] Zilhão M and Löffler F 2013 Int. J. Mod. Phys. A **28** 1340014 (*Preprint* [1305.5299](https://arxiv.org/abs/1305.5299))
- [39] Reisswig C and Pollney D 2011 Class.Quant.Grav. **28** 195015 (*Preprint* [1006.1632](https://arxiv.org/abs/1006.1632))
- [40] Ruiz M, Takahashi R, Alcubierre M and Nunez D 2008 Gen. Rel. Grav. **40** 2467 (*Preprint* [0707.4654](https://arxiv.org/abs/0707.4654))
- [41] Ferguson D, Anne S, Gracia-Linares M, Iglesias H, Jan A, Martinez E, Lu L, Meoni F, Nowicki R, Trostel M L, Tsao B J and Valorz F 2023 arXiv e-prints arXiv:2309.00653 (*Preprint* [2309.00653](https://arxiv.org/abs/2309.00653))
- [42] Schnetter E, Hawley S and Hawke I 2016 Carpet: Adaptive Mesh Refinement for the Cactus Framework (*Preprint* [1611.016](https://arxiv.org/abs/1611.016))
- [43] Higginbotham K, Khamesra B, McInerney J P, Jani K, Shoemaker D M and Laguna P 2019 Phys. Rev. D **100**(8) 081501 URL <https://link.aps.org/doi/10.1103/PhysRevD.100.081501>
- [44] Moore C J, Cole R H and Berry C P L 2014 Classical and Quantum Gravity **32** 015014 ISSN 1361-6382 URL <http://dx.doi.org/10.1088/0264-9381/32/1/015014>
- [45] Wette K 2020 SoftwareX **12** 100634
- [46] Kokkotas K D and Ruoff J 2001 Astronomy & Astrophysics **366** 565–572 (*Preprint* [gr-qc/0011093](https://arxiv.org/abs/gr-qc/0011093))
- [47] Berti E, Cardoso V and Will C M 2006 Phys. Rev. D **73** 064030 (*Preprint* [gr-qc/0512160](https://arxiv.org/abs/gr-qc/0512160))